

1 **T-cell potential for CD19-expressing malignancies revealed by multi-dimensional single-cell**
2 **profiling**

3 Ali Rezvan¹, Gabrielle Romain¹, Mohsen Fathi², Darren Heeke³, Melisa Martinez-Paniagua¹, Xingyue
4 An¹, Irfan N Bandey¹, Arash Saeedi¹, Fatemeh Sadeghi¹, Kristen Fousek⁴, Nahum Puebla-Osorio⁵,
5 Laurence J.N. Cooper², Chantale Bernatchez⁶, Harjeet Singh⁷, Nabil Ahmed⁴, Mike Mattie³, Adrian
6 Bot³, Sattva Neelapu⁵, and Navin Varadarajan^{1*}

7 ¹Department of Chemical and Biomolecular Engineering, University of Houston, Houston, Texas
8 77204, USA

9 ²CellChorus, Houston, Texas 77023, USA

10 ³Kite, a Gilead Company, Santa Monica, California 90404, USA

11 ⁴Texas Children's Hospital, Baylor College of Medicine, Houston, Texas 77030, USA

12 ⁵Department of Lymphoma and Myeloma, The University of Texas MD Anderson Cancer Center,
13 Houston, Texas 77030, USA

14 ⁶Department of Biologics Development, The University of Texas MD Anderson Cancer Center,
15 Houston, Texas 77030, USA

16 ⁷Division of Pediatrics, The University of Texas MD Anderson Cancer Center, Houston, Texas 77030,
17 USA

18 *To whom correspondence should be addressed:

19 Navin Varadarajan

20 Department of Chemical and Biomolecular Engineering

- 21 University of Houston
- 22 Houston, Texas 77204, USA
- 23 Tel: +1-713-743-1691;
- 24 E-mail: nvaradar@central.uh.edu

25 **ABSTRACT**

26 Adoptive immunotherapy with T cells expressing chimeric antigen receptors (CARs) for B-cell
27 malignancies serves as a model for identifying subsets with superior clinical activity. We profiled
28 the infusion products (IP) of 16 patients with large B-cell lymphoma (LBCL) using an integrated
29 suite of single-cell assays to reveal the therapeutic potential of CD19-specific CAR⁺ T cells.
30 Timelapse imaging microscopy in nanowell grids (TIMING) profiling revealed that T cells from
31 responders showed migration (persistent motion for at least one body length), and migration was
32 associated with serial killing capacity. In addition, confocal microscopy revealed that migration is
33 linearly correlated with both mitochondrial volume and lysosomal volume; and scRNA-seq
34 demonstrated that T cells from responders were enriched in pathways related to T-cell killing,
35 migration and actin cytoskeleton, and TCR clustering. A marker-free sorting strategy enriched T
36 cells with migratory capacity and validated serial killing, bioenergetics, and in vivo efficacy. In
37 aggregate, we demonstrate that migration is a cell-intrinsic biomarker independent of CAR design
38 or biomanufacturing, desired in the bioactivity of CAR⁺ T cells associated with clinical antitumor
39 efficacy.

40 INTRODUCTION

41 The ability to migrate to and within tissues differentiates effective T-cell therapeutics from other
42 targeted immunotherapies infusing recombinant proteins or small molecules. Few tools are
43 available to examine the migratory properties of T cells despite migration being a central feature
44 of their ability to recycle effector functions throughout malignant masses. The administration of
45 immune effector cells propagated ex vivo has been shown to be effective for the treatment of solid
46 tumors such as melanomas and liquid tumors such as acute and chronic B-cell leukemias^{1,2}. T cells
47 stably endowed with a genetically encoded chimeric antigen receptor (CAR) targeting CD19 have
48 shown remarkable clinical responses in B-lineage leukemias and lymphomas patients who were
49 refractory to other treatments. This has spurred the development of CARs targeting antigens other
50 than CD19 to treat hematologic malignancies and invasive cancers³⁻⁵. The field of CAR T cells has
51 exploded with the culmination of the Food and Drug Administration (FDA) approval of CAR T cell
52 products, and while attention has been devoted to antigen discovery and CAR design^{2,3,6},
53 identifying metrics that define the functional potential and thus the therapeutic prospects of T-cell
54 products is limited^{7,8}.

55 Because of inter- and intra-tumor heterogeneity, technologies that aggregate T-cell
56 biology are unable to accurately capture the complexities of an IP with defined and desired
57 characteristics. For example, populations of less differentiated cells (central memory [T_{CM}] or stem
58 memory [T_{SCM}] T cells) have increased proliferative capacity leading to sustained presence, but
59 individual cells vary in their persistence and functional potential⁹⁻¹¹. Although persistence of
60 infused T cells correlates with anti-leukemias effects, recent pre-clinical data suggest that the
61 ability of cells to recycle effector function within the tumor microenvironment (TME) is an essential

62 attribute for tumor eradication^{12,13}. We hypothesized that functional single-cell profiling of IPs by
63 quantifying the dynamics of T cells interacting with tumor cells would reveal properties of T cells
64 associated with antitumor efficacy and clinical benefit.

65 To test this hypothesis, we performed multi-omic dynamic profiling to understand the
66 heterogeneity of individual CD19-specific CAR T cells within axicabtagene ciloleucel (axi-cel) IP
67 administered to patients with LBCL. By integrating function, phenotype, transcriptional profiling,
68 and metabolism, we have identified that migration is a feature of T cells associated with clinical
69 response and that migration is associated with bioenergetically fit cells with serial killing
70 functionality. The link between persistent migration and killing is preserved across different CAR
71 designs and manufacturing protocols, and provides new insights into the cellular attributes of T
72 cells essential for efficacy.

73 **RESULTS**

74 **Migratory T cells are enriched in CAR T cell infusion products (IPs) associated with clinical**
75 **responses.** To investigate the importance of CAR T cells characteristics, we used cells from infusion
76 products of patients with Diffuse Large B cell Lymphoma (DLBCL) who received anti-CD19 CAR T
77 cell therapy. In total, samples from 16 patients were collected and tested at the single-cell level
78 using TIMING, confocal microscopy, and single-cell RNA sequencing (**Figure 1**). At 3-months
79 follow-up after the treatment, 10 patients had a complete response (CR), and 6 showed either
80 partial response or progressive disease (PR/PD).

81 Phenotypic characterization of the CAR T cells by flow cytometry showed no differences in
82 frequency of CAR expression [40-80%] and a balanced CD4/CD8 distribution (**Figure S1A-B**). We
83 used the TIMING platform to dissect functional heterogeneity at the single-cell level across these
84 16 IPs. At an effector-to-target (E:T) of 1:1, the frequency of T cells establishing a synapse or killing
85 the engaged tumor cells was not different between IPs associated with any clinical response (**Table**
86 **ST1, Figure S2A** and **Movie M1**). At the single-cell level, the dynamics of the interaction between
87 the T-cell and the tumor cell leading to killing were largely conserved, consistent with the
88 expectation that intrinsic T-cell killing mechanisms are not different between the two groups of
89 responders (**Figure S2C**). We next evaluated the ability of T cells to recycle effector (lysis) function
90 by examining nanowells with 1E:2T and observed that the frequency of serial killer T cells was
91 significantly enriched in IPs associated with clinical response (**Figure 2A, Figure S2B, Movie M2**
92 and **Movie M3**).

93 T cell based drugs need to actively migrate to seek and destroy tumors. We accordingly
94 measured the migratory potential of T cells using TIMING. In nanowells that lacked tumor cells

95 (1E:0T), the average T-cell migration (persistent motility for at least one body-length, hereafter
96 migration) was significantly increased in IPs associated with CR (**Figure 2B**). Aggregated by
97 response, T cells from patients with CR showed a significantly faster migration compared to T cells
98 from patients with PR/PD at single-cell level (**Figure 2B** and **Movie M4**). Similarly, even within
99 1E:1T nanowells, single T cells from patients with CR showed enhanced migration both with and
100 without conjugation to tumor cells, compared to T cells from patients with PR/PD (**Figure 2C** and
101 **Movie M5**). We next pooled T cells from all IPs (1E:1T nanowells, regardless of clinical response)
102 and this comparison confirmed that migration is an intrinsic feature of killer T cells compared with
103 non-killer T cells (**Figure 2D** and **Movie M6**).

104 In vivo proliferative capacity leading to cellular persistence after infusion is one of known
105 correlates of CAR T cells¹⁴. We integrated TIMING with 3D confocal microscopy to interrogate the
106 correlation between migration, killing, and proliferative capacity within IP T cells. We constructed
107 the image of each cell as a series of stacks in 3D to capture the mitochondrial volume (known
108 feature of proliferative capacity)¹⁴, lysosomal volume (killing capacity), and the nucleus (cell size).
109 When the T cells from the IPs were stratified by clinical response, T cells from CR patients had
110 increased mitochondrial and lysosomal volume in comparison with T cells from PR/PD patients
111 (**Figure 2E**). Since IP T cells from each patient had been characterized by both TIMING and confocal
112 microscopy, we investigated the correlation between migration, mitochondrial and lysosomal
113 volumes. We observed a strong linear correlation between migration and mitochondrial mass
114 (Pearson correlation 0.62, P value = 0.01), and between migration and lysosomal volume (Pearson
115 correlation 0.66, P value = 0.006) (**Figure 2F**). We performed unsupervised hierarchical clustering
116 of all the dynamic parameters from TIMING, and the organelle measurements from confocal

117 microscopy. Clustering showed that serial killing, migration, mitochondrial volume and lysosomal
118 volume were features associated with T cells from patients who achieved CR (**Figure S2D**).
119 Collectively, these single-cell measurements illustrate that IP T cells from patients with CR, balance
120 migration, serial killing and cellular fitness.

121 **ScRNA-seq identifies a core signature of migration in IP T cells from patients who achieved**
122 **CR.** To understand the molecular basis of these observations, we performed scRNA-seq of 21,469
123 T cells from nine of these patients (5 CR, 4 PD) for whom we had access to additional T cells from
124 the IPs. To minimize batch effects, we barcoded samples in sets of three, prepared libraries and
125 sequenced them together. We defined ten clusters of T cells (T1-10) based on their molecular
126 properties and cells derived from patients with both CR and PD were represented in all the clusters
127 (**Figure 3A**). Consistent with previous reports, the CAR transcript was distributed in all of these
128 different clusters, but the overall frequency of the detected transcript was lower than CAR
129 expression by flow cytometry, suggesting a high rate of dropout of the CAR transcript (**Figure**
130 **S1A**)⁸. Accordingly, we performed subsequent analyses on all T cells from IPs.

131 We did not observe a significant expression of either well-established genes associated
132 with T-cell exhaustion including *TOX*, *PDCD1*, *TIGIT*, and *CD38*; or emerging regulators like *ID3*
133 and *SOX4*, within any of our T cells clusters (**Figure S3A**)^{8,15}. We next focused the analysis on CD8⁺
134 T cells. Using multi-omic dynamic profiling of healthy donor-derived CD19-specific CAR T cells, we
135 have recently published a molecular signature of both non-killer and persistent serial killer CD8⁺ T
136 cells¹⁶. We performed single-cell gene set enrichment analysis (ssGSEA) and showed that
137 consistent with our functional data (**Figure 2A**), serial killer T cells were significantly enriched in
138 IPs from patients with CR whereas non-killers were significantly enriched in IPs from patients with

139 PD (**Figure 3B**). CD8⁺ T cells from patients who achieved CR also showed enrichment in a *TCF7*
140 gene signature (**Table ST2**) associated with enhanced in vivo persistence compared to CD8⁺ T cells
141 from patients with PD (**Figure 3C**)¹⁷. We next identified differentially expressed genes (DEGs)
142 between CD8⁺ T cells from IPs that resulted in CR compared to IPs of patients with PD. We
143 performed unsupervised clustering based on the DEGs and identified seven clusters (**Figure S3B**).
144 Clusters CD8_1 and CD8_2 were predominantly comprised of cells from PD, whereas clusters CD8_6
145 and CD8_7 were predominantly comprised of cells from CR (**Figure 3D**). Cells within the CD8_6
146 cluster showed a high expression of genes associated with effector functionality including
147 cytotoxicity (*GZMB*, *PRF1*, *FASLG*, and *NKG7*), cytokine and chemokines (*CCL3-5*, *IFNG*), and
148 migration (*MYH9*, *RHOH*, and *RHOC*) (**Figure 3E**). Cells in clusters CD8_6 and CD8_7 were
149 significantly enriched in pathways associated with TCR activation ($p < 5 \times 10^{-315}$), PGC1A and
150 mitochondrial biogenesis ($p < 1 \times 10^{-52}$), actin cytoskeleton regulation ($p < 8 \times 10^{-53}$) and migration
151 (RHO pathway, $p < 4 \times 10^{-242}$) (**Figure 3D**). This overlap between TCR activation, cytotoxicity and
152 migration at the single-cell level is consistent with the known immunobiology of T cells, the same
153 genes that control cellular migration also control cytoskeletal remodeling at the immunological
154 synapse.

155 To map specificity to T cell migration, we curated a collection of 40 genes (labeled T-cell
156 migration score, **Table ST2**) with documented roles in actin cytoskeleton remodeling in T cells¹⁸
157 including *RHOA* and *MYH9* (actomyosin contraction), *TLN1* and *VCN* (actin-integrin interplay), and
158 *MYO1G* (actin contraction). ssGSEA confirmed that the T-cell migration score was significantly
159 enriched in the CD8_6 and CD8_7 clusters compared to the CD8_1 and CD8_2 clusters ($p < 5 \times 10^{-$
160 ¹⁴⁶) (**Figure S3B**). CD8⁺ T cells from patients who achieved CR showed a significant enrichment in

161 the T-cell migration score compared to CD8⁺ T cells from patients who associated with PD (**Figure**
162 **3F**). It has been recently reported that T-cell migration signatures can also be associated with T-
163 cell exhaustion¹⁹. Within our dataset, the T cells, regardless of response status, did not show
164 significant expression of the genes associated with the migration/exhaustion phenotype including
165 *CD38*, *MYO7A*, *MYO7B*, or *CAV1* (**Figure S3A**).

166 We next analyzed CD4⁺ T cells and first confirmed that CD4⁺ T cells from patients who
167 achieved CR showed a significant enrichment in the T-cell migration score compared to CD4⁺ T
168 cells from patients who associated with PD (**Figure 3F**). Analysis of the DEGs and unsupervised
169 clustering of the CD4⁺ T cells revealed nine clusters (**Figure S3C**). Two clusters, CD4_1 and CD4_2,
170 predominantly comprised cells from PD, whereas clusters CD4_8 and CD4_9 were predominantly
171 comprised of cells from CR (**Figure 3G**). In contrast to the CD8⁺ T cell clusters, genes for immediate
172 cytotoxicity were not high in CD4_8 and CD4_9; rather these clusters showed an enrichment of
173 genes associated with long-term in vivo persistence including *LEF1*, *TCF7*, *CD27*, and *IL7R* (**Figure**
174 **3H**). In aggregate, scRNA-seq revealed that CD8⁺ T cells from IPs with CR are enriched in serial
175 killers and associated with immediate cytotoxicity whereas CD4⁺ T cells from IPs with CR are
176 associated with long-term persistence. This divergence in function and long-term in vivo
177 persistence is well-supported by other pre-clinical and recent long-term follow-up clinical data^{20,21}.
178 Importantly, scRNA-seq revealed that migration is an intrinsic property of both CD4⁺ and CD8⁺ T
179 cells associated with clinical responses.

180 **T-cell migration enables selection of functional T cells.** Based on our results of profiling clinical
181 IPs, we next wanted to identify if migration can serve as a biomarker to identify the fittest cells for
182 adoptive immunotherapy. We sought proof-of-concept studies based on defined populations of

183 healthy donor-derived CD19-specific CAR T cells to utilize migration as a selectable property for
184 T-cell bioactivity. We hypothesized that T cells with migration could be enriched using a modified
185 transwell assay, with pore sizes consistent with previously published confinement studies of T cells
186 in vitro²². We initially tested the effect of functionalization of the membrane by coating it with
187 fibronectin or collagen, but in comparison with the uncoated membrane, these did not significantly
188 alter the number of migrated (migratory) cells (not shown).

189 Unstimulated CD19-specific CAR⁺ human T cells with CD28 endodomain (designated 19-
190 28z), comprised of both CD4⁺ and CD8⁺ T cells, were seeded onto a Boyden chamber, and
191 migratory T cells were harvested from the bottom chamber and compared to cells from the top
192 chamber (non-migratory) or unsorted cells (**Figures S4** and **S5**). TIMING confirmed that the cells
193 harvested from the bottom chamber had an increased frequency of individual T cells with
194 migration in comparison to the cells harvested from the top chamber, confirming that at least for
195 proof-of-concept studies the modified transwell assay could be utilized to enrich T cell populations
196 based on the migration (**Figure 4A**). To dissect the cytotoxic capacity at the single-cell level, we
197 performed TIMING assays with migratory or non-migratory 19-28z T cells as the effector cells and
198 NALM-6 cells as targets. Consistent with the data from the clinical IPs, migratory T cells participated
199 in killing and serial killing at significantly higher frequencies in comparison to the non-migratory
200 population (**Figure 4B**). Since we recognized that the TIMING data is gated based on T cells that
201 conjugate to tumor cells (*i.e.* ones that establish a synapse), and posited that migration is likely to
202 impact the ability of T cells to seek and conjugate to tumor cells, we modeled the time evolution
203 of the interaction and outcomes of the interaction between individual T cells and tumor cells using
204 a state transition diagram. Consistent with our hypothesis, the most probable path for migratory

205 T cells was to encounter multiple tumor cells and behave as serial killers, whereas non-migratory
206 T cells were characterized by an impediment in conjugating to tumor cells (**Figure 4C**). Collectively,
207 these results suggest that the migratory T cells isolated by the transwell assay were enriched in
208 serial killers.

209 **Migratory T cells have a high spare respiratory capacity (SRC) but are phenotypically similar**
210 **to the unsorted T cell populations.** We next sought to determine if the sorted migratory 19-28z
211 T cells, marked the subpopulation with superior efficacy, and to define the properties that
212 distinguished the migratory population from the parent, unsorted population. To test if the
213 differences in the migration and functional properties of migratory T cells could be explained by
214 their phenotype, we compared the memory phenotype of migratory and unsorted T cells, and
215 observed that both populations were comprised predominantly of naïve ($CD62L^+CD45RA^+$) and
216 central memory ($CD62L^{neg}CD45RA^+$) CAR^+ T cells (**Figure 5A** and **Figure S5**). Both migratory and
217 unsorted populations had no difference in expression of either the CAR or intracellular Granzyme
218 B (**Figure S5** and **Figure 5B**), consistent with transcriptional and functional data from IP profiling.

219 Migration is an energy intensive process and the data from profiling the IPs suggested that
220 migration in serial killer T cells is also correlated with increased metabolic fitness. To directly
221 establish a link between migration and metabolism, we measure the oxygen consumption rate
222 (OCR) of both the migratory and unsorted T-cell populations. Metabolic flux analyses revealed that
223 the migratory populations had both higher maximal respiratory capacity and spare respiratory
224 capacity (SRC) in comparison with either the unsorted or non-migrated T-cell populations (**Figure**
225 **5C**). Since the data from IPs suggested differences in mitochondrial volume, we utilized 3D single-
226 cell confocal microscopy to study mitochondrial structure. Imaging of single cells confirmed that

227 migratory 19-28z T cells had increased mitochondrial volume and an increased number of
228 punctate mitochondria (consistent with fission) in comparison to the non-migratory 19-28z T cells
229 (**Figure 5D**). Since AMP-kinase (AMPK) is a well-known regulator of mitochondrial mass and
230 integrity, we next sought to determine if the kinase activity of activated AMPK (phosphorylation in
231 the α -subunit) was the molecular link between migration and metabolism that we have
232 documented. Accordingly, we inhibited the activity of AMPK in 19-28z T cells using the small
233 molecule inhibitor dorsomorphin (compound C, CC). Cells treated with CC showed profound
234 defects in morphology and migration, confirming that AMPK activity is essential for the migration
235 of T cells (**Figure 5E-F**). Consistent with impaired migration, CC treated 19-28z T cells showed a
236 decreased propensity to conjugate to tumor cells in single cell assays, in comparison to DMSO-
237 treated 19-28z T cells (**Figure S6A**). Furthermore, treated 19-28z T cells that did make contact with
238 target cells showed significantly longer conjugation times and delayed induction of tumor cell
239 apoptosis when compared to the untreated 19-28z T cells (**Figure S6B** and **Figure 5G**). We also
240 confirmed that this requirement of AMPK for migration was generalizable to genetically
241 unmodified, tumor-reactive T cells and not just CAR⁺ T cells (**Figure S7** and **Movie M7**).
242 Collectively, these results show that transwell-sorted 19-28z T cells phenocopy the functional
243 properties of T cells from patients who achieved CR: migration, serial killing, and mitochondrial
244 fitness.

245 **Migratory T cells reject established leukemia and sustain persistence in vivo.** Based on the in
246 vitro functional and bioenergetics data, we hypothesized that migratory T cells should be able to
247 promote CAR⁺ T-cell persistence in vivo leading to improved antitumor efficacy. We assessed the
248 efficacy of the migratory 19-28z T cell population using a model of established leukemia. NOD.Cg-

249 Prkdcscid Il2rgtm1Wjl/SzJ (NSG) mice were injected with CD19⁺ NALM-6 transduced with firefly
250 luciferase (ffLuc), and after confirming the engraftment of tumor, we treated the mice with 19-28z
251 CAR⁺ T cells (**Figure S8**). The migratory 19-28z T cells demonstrated potent and superior antitumor
252 activity, reducing tumor burden to the detection limit, with tumor flux significantly lower in
253 comparison to the unsorted 19-28z T cells (**Figure 6A-B**). It is worth emphasizing that this
254 improvement in efficacy was obtained purely by isolation of the subpopulation of migratory cells
255 in the population without any additional culturing or modifications. In both the bone marrow (BM)
256 and spleen, mice treated with migratory 19-28z T cells harbored no tumor cells, but only persisting
257 CAR⁺ T cells (**Figure 6C**). By contrast, we could detect the outgrowth of tumor cells within the BM
258 of mice treated with unsorted 19-28z T cells, which was accompanied by a low frequency of CAR⁺
259 T cells in the BM in these same mice (**Figure 6C**). Similarly, while we could detect CAR⁺ T cell
260 persistence in the spleen of mice infused with migratory 19-28z T cells, there were very low
261 frequencies of CAR⁺ T cells in the spleen of the mice that received the unsorted 19-28z T cells
262 (**Figure 6C**). In an independent experiment, we compared the efficacy of migratory and unsorted
263 19-28z T cells at suboptimal doses against these same NALM-6 tumors in vivo; migratory 19-28z
264 T cells showed enhanced antitumor activity compared to the unsorted 19-28z T cells (**Figure S9**).
265 In aggregate, these results demonstrate that migration is a desired biomarker indicative of
266 subpopulations of T cells with desired function and in vivo persistence.

267 **Migration is a biomarker of functional T cells independent of CAR design or**
268 **biomanufacturing protocols.** We next tested if the link between migration and functionality is
269 generalizable to CD19-specific CARs derived from diverse manufacturing protocols, and against
270 multiple tumor targets. Accordingly, we utilized TIMING to first compare the migration of killer

271 and non-killer CAR⁺ T cells electroporated and manufactured with a CD19-specific CAR containing
272 the CD8 hinge and transmembrane regions (19-8-28z) (**Figure 7A**). Consistent with our other data,
273 individual killer 19-8-28z T cells demonstrated higher migration both with and without conjugation
274 to NALM-6 tumor cells compared with non-killer 19-8-28z T cells (**Figure 7B** and **S10A**). Next, we
275 tested two tri-specific CAR⁺ T cells designed for mitigating CD19 escape in primary ALL (**Figure 7C**
276 and **7E**)²³. These tri-specific CAR⁺ T cells were retrovirally transduced, the CAR design incorporated
277 a 41BB endodomain, and the T cells were expanded (anti-CD3/CD28 and IL7/IL5), as described
278 previously²⁴. We tested these T cells against patient-derived tumor cells. Again, by comparisons
279 using TIMING, individual killer CAR⁺ T cells demonstrated higher migration both with and without
280 conjugation to patient-derived tumor cell lines compared with non-killer CAR⁺ T cells (**Figure 7D**,
281 **7F** and **Figure S10B-C**). These data suggest that the link between migration and killing can be
282 preserved across multiple CAR designs and manufacturing protocols.

283 **DISCUSSION**

284 With the approval of CD19-specific CAR⁺ T cells as living drugs, there is a need to define
285 biomarkers that provide insights into the clinical impact of adoptive immunotherapy. Identifying
286 cellular properties associated with clinical efficacy are important for ensuring predictable clinical
287 outcomes and for defining the desirable attributes during biomanufacturing. Our results
288 demonstrate that the variability in IP can directly impact clinical efficacy and that migration feature
289 can be used to identify serial killer T cells with enhanced in vivo persistence. Prior studies of IPs
290 have been limited to static profiling based on flow cytometry²⁵, whole-transcriptome profiling^{8,25},
291 or cytokine secretion⁷, but our dataset is the first multi-omic profile that includes dynamic imaging
292 across thousands of T cells and their interactions with tumor cells. Our discovery of migration as a
293 cellular biomarker of T cells with in vivo persistence is consistent with pre-clinical studies using
294 two-photon microscopy that demonstrated: (1) mouse T-cell migration prior to engagement and
295 killing of tumor cells is an essential component of their efficacy^{26,27}, (2) both CD4⁺ and CD8⁺ CAR⁺
296 T cells mediate direct and indirect cytotoxicity upon migration to the tumors²⁸, (3) migratory T cells
297 are long-duration tumor-resident T cells¹⁹, (4) functional exhaustion by PD-1 induces T cell
298 migration paralysis and blockade of PD-1 can restore T cell migration and function²⁹, and (5) T-cell
299 migration in tissue increases with serial killing and tumor rejection³⁰. This ability of intrinsic T cell
300 migration to promote tumor exploration is a central feature of cells as drugs that distinguishes
301 them from small molecule and protein therapeutics³¹. At the molecular level, the genes/proteins
302 involved in migration, including *RHOA*, *RAC1*, and *CDC42*, affect multiple aspects of T-cell
303 immunobiology, including cell polarity, chemotaxis, synapse formation, signaling, and effector
304 responses; and hence it is not surprising that migration is a biomarker for cells with optimal effector

305 functionality³². From a translational perspective, T cells from leukemia/lymphoma patients are
306 known to harbor defects in migration and immunological synapse formation³³⁻³⁵. Since the FDA
307 approved immunomodulatory drug, lenalidomide is known to rescue some of these defects, it will
308 be important to quantify if addition of drugs like lenalidomide during CAR T cell manufacturing
309 can yield fitter migratory cells with superior anti-tumor efficacy^{34,36,37}.

310 T cells exhibiting migration have a high bioenergetic requirement to support locomotion.
311 Our results confirmed that the migratory CAR T cells had enhanced mitochondrial SRC, a property
312 that likely promotes long-term survival^{38,39}. 3D confocal microscopy also demonstrated increased
313 punctate mitochondria in individual cells with migration. Within this context, since AMPK is a well-
314 known master regulator of SRC and mitochondrial remodeling, we confirmed that inhibiting AMPK
315 has a profound impact on T-cell migration and consequently function at the single-cell level. To
316 the best of our knowledge, this is the first direct demonstration of the role of AMPK in T-cell
317 migration at the single-cell level, and this sets the stage for additional studies that explore this link
318 between AMPK as a modulator of energetics and function within individual T cells and their
319 antitumor efficacy. Our data is also consistent with studies that have demonstrated activated AMPK
320 as a negative regulator of cellular adhesion and integrin activity in other cell types, but it is also
321 important to recognize that AMPK is a global modulator of many different aspects of cell biology
322 that need to be mapped within the context of T cells^{40,41}.

323 An important question to consider in the context of IPs is how T-cell differentiation status
324 impacts the migratory potential of T cells. Within our IP CD8⁺ T cells, scRNA-seq revealed that
325 cluster CD8_6, enriched in CRs (**Figure 3**), has signatures of proliferation, migration and
326 cytotoxicity. We compared these signatures to known T-cell differentiation signatures with the aid

327 of STARTRAC (Single T-cell Analysis by Rna-seq and Tcr TRACKing)⁴². STARTRAC performs paired
328 scRNA-seq and TCR profiling (tracking clonotypes) to identify the properties of T cells that migrate
329 and expand in the tumor relative to paired normal tissue/lymph nodes^{42,43}. STARTRAC analyses of
330 mouse and human colon/breast cancers have revealed that the migratory T cells are highly
331 cytolytic and capable of expansion (similar to cells in cluster CD8_6), and are consistent with the
332 T_{EM} phenotype⁴²⁻⁴⁴. This needs to be interpreted with caution however, since as our sorting strategy
333 with healthy donor-derived CAR T cells illustrates, migratory T cells are not confined to a single T-
334 cell differentiation state. In comparing the signatures of CD4 and CD8 T cells within IP associated
335 with clinical responses, a different hypothesis arises. While signatures of CD8 T cells are associated
336 with immediate antitumor function including cytotoxicity, CD4 T cells signatures are primed for
337 long-term persistence. Collectively, these data present a testable hypothesis of division of labor
338 between the T cell subsets, and are consistent with emerging data for the role of CD4 CAR T cells
339 in long term durable responses^{21,45}.

340 Our results portray that migratory CAR T cells with increased bioactivity and functionality
341 lead to persistence in vivo and control of tumor growth. There are, however, limitations to our
342 study. We recognize that while the migration of these CAR⁺ T cells is a selectable property and
343 reflective of the bioactivity of cells within a given population, it is unknown whether migration by
344 itself can be utilized as a comparative marker in evaluating CAR⁺ T cell populations with varied
345 CAR designs. Furthermore, while we have demonstrated the implementation of a simple transwell
346 assay for the enrichment of migratory 19-28z T cells, as the data demonstrates, the segregation of
347 cellular populations can be improved. For translational purposes, we anticipate building
348 microfluidic chips capable of efficient segregation of large numbers of migratory T cells⁴⁶. Lastly,

349 while we recognize that migration might not necessarily be imprinted on T cells and their daughter
350 cells, as they undergo cell division in vivo, migration nonetheless enables the identification and
351 isolation segregation of T cells in vitro with long-lived potential in vivo.

352 In summary, we identified that migration is a marker that selects for T cells with superior
353 antitumor effects reflective of productively activated cells with a balanced ability for functional
354 execution without compromising proliferative potential. These attributes can be used to help
355 improve manufacturing of T cells leading to predictable and superior patient clinical outcomes.

356

357 **METHODS**

358 **Human subject statement.** All work outlined in this report was performed according to protocols
359 approved by the Institutional Review Boards at the University of Houston and the University of
360 Texas MD. Anderson Cancer Center. TIL cells were expanded from surgical resection tissue under
361 the protocol (2004–0069) approved by the Institutional Review Board (IRB) of the University of
362 Texas MD Anderson Cancer Center (Houston, TX) and an FDA-approved Investigational New Drug
363 (IND) application (NCT00338377).

364 **Patient samples.** Patients with diffuse large B cell lymphoma (DLBCL) were treated with anti-CD19
365 CAR T cells. CAR T cells were made by Kite Pharma (Los Angeles, CA). After CAR T cell infusion,
366 leftover cells in infusion bags were collected and transferred to the laboratory for microscopy
367 assays and scRNA sequencing. At the 3-months follow-up, 10 patients showed complete response
368 (CR, 62%), 2 showed partial response (PR, 13%) and 4 showed progressive disease (PD, 25%).

369 **Cell lines and primary T cells.** Human pre-B cell leukemic line NALM-6 (ATCC) were cultured in
370 T-cell medium (RPMI + 10% FBS) and used as CD19⁺ target cells. A second-generation CAR
371 signaling via CD28 and CD3- ζ endodomains (with a mutated IgG4 spacer) were expressed in
372 human T cells by electroporation with DNA plasmids from the *Sleeping Beauty* (SB)
373 transposon/transposase system, as described previously¹¹. T cells were used 2-3 weeks after
374 transfection.

375 **Nanowell array fabrication.** Nanowell array fabrication to investigate the effector functions at
376 single-cell level was performed as described previously^{47,48}. Briefly, we designed a master template
377 of nanowell array using AutoCAD (Autodesk) and fabricated it on a silicon wafer using soft
378 lithography techniques. We made the nanowell array by pouring Polydimethylphenylsiloxane

379 (PDMS) on the silicon wafer and spinning the silicon wafer using a spin coater and then baking it
380 at 70°C for 2 h. Then, we plasma oxidized the nanowell and attached it to the bottom of a 50-mm
381 glass bottom Petri dish. Nanowell array had hundreds of nanowells, and each well was 50 μm \times 50
382 μm \times 50 μm in size.

383 ***TIMING assays to profile functionality at single-cell level.*** We labeled approximately 1 million
384 CAR T cells with PKH67 green fluorescent dye (Sigma) and 1 million NALM-6 cells with PKH26 red
385 fluorescent dye (Sigma) as per the manufacturer's protocol. We loaded both CAR T cells and
386 NALM-6 cells on nanowell array in the way to reach mainly one effector and one to two targets
387 per nanowell (E:T=1:1 or 1:2). We used complete cell-culture media (IMDM + 10% FBS) to cover
388 the nanowell array. We added Annexin V-Alexa Fluor 647 (AF647) (Invitrogen™) to the covering
389 media to detect cell apoptosis during the experiment.

390 We used an inverted fluorescent microscope (Zeiss) which was equipped with a Lambda-
391 DG4 illumination system, differential interference contrast (DIC) condenser annulus, 20 \times 0.80 NA
392 Zeiss Plan-Apochromat objective and Orca Flash 4.0 camera (Hamamatsu). We placed the petri
393 dish containing the PDMS-nanowell array, on a motorized stage in a box to maintain the
394 temperature at 37°C and CO₂ level at 5%. We used Alexa Flour (488 nm), TexasRed (566 nm) and
395 Cy5 (651 nm) channels for detection of CAR T cells, NALM-6 cells, and apoptosis, respectively.
396 Images were acquired for six hours with five-minute intervals.

397 ***Confocal microscopy for integrated measurements of subcellular organelles.***

398 For confocal microscopy, we fluorescently labeled ~300,000 CAR T cells at 37°C for 30 minutes in
399 1:1 (v/v) solution of live cell staining buffer (Abcam) and RPMI-1640 (Corning) containing final
400 concentrations of 500 nM MitoTracker™ Deep Red FM (Invitrogen™), 250 nM LysoRed (Abcam)

401 and 1 μ M Hoechst 33342 (Sigma) for labeling mitochondria, lysosome, and nucleus, respectively.
402 Then we washed cells with Hanks' balanced salt solution (Cellgro) + 10% HEPES (Corning) and
403 resuspended in cell culture media (RPMI + 10% FBS), and then loaded labeled cells on a glass-
404 bottom 96 well plate (MatTek Corporation) for confocal imaging.

405 We used a Nikon A1/TiE inverted microscope equipped with a 100x, 1.45 NA objective for
406 imaging. We took 3D images (~50 slices, 0.3 μ m/slice) from multiple fields of view using DAPI
407 (404.0 nm), FITC (488.0 nm), TexasRed (561.8 nm) and Cy5 (641.0 nm) channels for detection of
408 nucleus, membrane, lysosome, and mitochondria, respectively.

409 ***Image processing, cell segmentation, cell tracking, and data analytics.***

410 For TIMING assay image processing, we used a home-made pipeline to analyze 16-bit images as
411 described before⁴⁹. Briefly, an automated pipeline was implemented for automatic detection of
412 nanowells, cell segmentation, tracking and feature computation. The pipeline output are the tables
413 containing statistical information for nanowells with one effector cell and up to five target cells
414 (1E:1T – 1E:5T). We partitioned events based on the functionalities of the cells i.e. 1E:1T-killing,
415 mono-killing and serial killing (**Figure S2A-B**):

- 416 a. 1E:1T killing: a single T cell killing a target cell existing in the nanowell upon conjugation.
- 417 b. Mono killing: a single T cell killing only one target cell upon conjugation, while multiple
418 targets (at least two) exist in the nanowell.
- 419 c. Serial killing: a single T cell killing at least two target cells upon conjugation, while multiple
420 targets (at least two) exist in the nanowell.
- 421 d. No killing: T cells without killing any target cells despite evidence of conjugation.

422 For tracking the mitochondria and lysosomes within the cells using confocal microscopy,
423 Z-stacks of 16-bit images were extracted for each channel and processed in ImageJ (National
424 Institutes of Health) using a series of plugins. First, the Subtract Background plugin was applied to
425 the mitochondria and lysosome channels prior to segmentation to reduce variations in
426 background intensities. Next, the 3D Objects Counter plugin was applied to the background-
427 corrected image to determine mitochondrial and lysosome regions of interest (ROIs). ROIs were
428 overlaid onto the original image and measurements were collected. Similarly, the 3D Objects
429 Counter plugin was used on nucleus channel using the original image only. Lastly, tracking of
430 single cell movement was done using the TrackMate plugin⁵⁰ to filter out unstable cells upon their
431 movement. All measurements were consolidated in R, where mitochondria and nuclei were
432 matched to their corresponding cell.

433 **Single cell RNA sequencing (scRNA-seq).** We performed scRNA-seq for nine samples (5 CR and
434 4 PD) with enough number of residual cells. We first used dead cell removal kit (Miltenyi Biotec,
435 Germany) containing MicroBeads for the magnetic labeling of dead cells and we then removed
436 the dead cells by passing the resuspended cells through the magnetic field of a MACS separator.
437 We performed library preparation process in three batches. For each batch, we used three different
438 TotalSeq C anti-human Hashtag Antibodies (BioLegend, San Diego, CA) to multiplex the samples
439 as per the manufacturer's protocols. Next, we did transcriptome and TCR capturing using 10x
440 Chromium platform (10x Genomics, Pleasanton, CA). We used Chromium single cell 5' reagent v2
441 kit for gene expression and V(D)J profiling. The sequencing was performed using a HiSeq PE150
442 sequencer (Illumina, San Diego, CA).

443 **ScRNA-seq analysis.** We processed gene expression FASTQ files generated with Illumina
444 sequencer using the Cell Ranger pipeline (version 6.0.0, 10x Genomics) for read alignment and
445 generation of feature-barcode matrices. The output files then were uploaded into R (version 4.0.1)
446 for further processing using Seurat Package (version 4.1.0)⁵¹. We used the SAVER package⁵² first,
447 to recover the gene expression profile in the data. Then we filtered out the cells with high
448 mitochondrial gene expression (more than 15% of the read counts) and we ended up with 21,469
449 cells from nine patients with mean unique molecular identifier (UMI) of 7738.

450 We detected the highly variable genes and significant principal components (PCs) following
451 the Seurat standard workflow for unsupervised clustering of the cells and used uniform manifold
452 approximation and projection (UMAP) for visualization of the clusters. We identified CD8 and CD4
453 T cell subsets using *CD8A*, *CD8B*, *CD4* and *CD40LG* gene markers. We identified CAR⁺ cells by
454 detection of the CAR sequence (FMC63-CD19scFV, GenBank: HM852952.1).

455 We used gene set variation analysis (GSVA) package⁵³ in R to calculate ssGSEA scores for
456 different pathways. We used pre-defined gene-sets from molecular signatures database (MSigDB,
457 v7.5.1) for pathway analysis. We also used customized gene-sets: TCF7.regulon¹⁷, T cell migration¹⁸,
458 CD4⁺ Ki67²¹ and CD8⁺ effector⁴² based on previous publications. Lowly expressed genes (average
459 expression <0.25) were removed from the pathway analysis. We generated heatmaps by pheatmap
460 package in R. We performed statistical analysis and generated *P* values in R.

461 **Migration of T cells through a transwell migration chamber.** Unstimulated, overnight serum
462 deprived, CAR⁺ T cells were seeded on the top compartment of PET five or eight μ m-pore Boyden
463 transmigration chamber (EMD Millipore), while the lower compartment contained FBS rich media.
464 After 4-6 hours, the cells from the bottom and the top compartment were harvested as "migratory"

465 and "non-migratory" populations, respectively. The lower part of the membrane was washed into
466 the "migratory" cell suspension, while the top surface of the membrane is washed into the "non-
467 migratory" cell suspension. We analyzed the phenotype and function of the cells using flow
468 cytometry and TIMING.

469 **Flow cytometry-based phenotyping.** For phenotyping, we stained the CAR⁺ T cells using a panel
470 of human-specific antibodies CD62L (DREG-56), CD45RA (HI100), CD3 (SK7), CD4 (OKT4), CD8
471 (RPA-T8) and Granzyme B (QA16A02) from Biolegend. The anti-CAR scFv was made in house⁵⁴. We
472 analyzed the cells using BD LSRFortessa X-20 cell analyzer.

473 **Compound C inhibition assays.** We incubated T cells with 10 μM dorsomorphin (Sigma Aldrich)
474 for a period of 6-24 hours. The T cells were subsequently used for either migration assays or
475 functional profiling using TIMING assays. Incubation with compound C did not have an impact on
476 T-cell viability (data not shown).

477 **In vivo efficacy of CAR⁺ T cells.** On day 0, 7-week-old NOD.Cg-PrkdcscidIl2rgtm1wjl/SzJ (NSG)
478 mice were injected intravenously (i.v.) via a tail vein with 1.5×10⁴ EGFP⁺ ffLuc⁺ NALM-6 cells. Mice
479 (n = 10/group) in the two treatment cohorts received via tail vein injection (on day 5) of 10⁷ CAR⁺
480 T cells. One group of mice (n = 10) bearing tumor were not treated with T cells. Anesthetized mice
481 underwent bioluminescent imaging (BLI) in an anterior-posterior position using a Xenogen IVIS
482 100 series system (Caliper Life Sciences) 10 minutes after subcutaneous injection (at neck and
483 shoulder) of 150 μL (200 μg/mouse) freshly thawed aqueous solution of d-Luciferin potassium salt
484 (Caliper Life Sciences) as previously described⁵⁵. Photons emitted from NALM-6 xenografts were
485 serially quantified using the Living Image 2.50.1 (Caliper Life Sciences) program. On day 28, five
486 mice in each group were euthanized to evaluate the presence of T cells and tumor cells. Bone

487 marrow was flushed from the femurs using 30Gx $\frac{1}{2}$ inch needles (BD, catalog no. 305106) with 2%
488 FBS in PBS. Spleens were disrupted using a syringe in 2% FBS/PBS and passed through a 40 μ m
489 nylon cell strainer (BD, catalog no. 352340) to obtain a single-cell suspension. Red blood cells from
490 bone marrow, spleen, and peripheral blood were lysed using ACK lysing buffer (Gibco-Invitrogen,
491 A10492) and remaining cells were stained for the presence of tumor (human CD19 and EGFP), T
492 cells (human CD3) and CAR T cells (scFv) by flow cytometry. The remaining five mice in each group
493 were used to determine the survival curves. In the suboptimal dose model, the mice were treated
494 exactly as above except that on day 5, 2×10^6 CAR⁺ T cells were injected intravenously.

495 ***Data visualization and statistical analysis.*** Data plotting and statistical analysis were performed
496 in R and GraphPad Prism v7. Schematics were made in Inkscape (v1.1.2).

497 **AUTHORSHIP CONTRIBUTION**

498 Designed the study: AR, GR, SN, LJNC, HS and NV

499 Prepared the manuscript: AR, GR, MF, HS, SN, NV and LJNC

500 Performed experiments: AR, GR, MF, MMP, KF, XA, FS and IB

501 Analyzed data: AR, GR, MF, AS, MMP, XA, NA and FS

502 Provided patient samples: HS, LJNC, SN, NPO, AB, CB, MM and DH

503 All authors edited and approved the manuscript.

504 **ACKNOWLEDGEMENTS**

505 This publication was supported by the NIH (R01GM143243); CPRIT (RP180466); MRA Established

506 Investigator Award to NV (509800), NSF (1705464); CDMRP (CA160591); and Owens foundation.

507 We would like to acknowledge the MDACC Flow Cytometry and Cellular Imaging Core facility for

508 the FACS sorting (NCI P30CA16672), Intel for the loan of computing cluster, and the UH Center for

509 Advanced Computing and Data Systems (CACDS) for high-performance computing facilities.

510

511 **FINANCIAL DISCLOSURE**

512 LJC and NV are co-founders of CellChorus that licensed TIMING from University of Houston.

513 LJC has equity ownership in Alaunos Oncology (formerly Ziopharm Oncology). The SB system for

514 CD19-specific CAR⁺ T cells is licensed including to Ziopharm Oncology. MF is an employee of CC.

515 None of these conflicts of interest influenced any part of the study design or results.

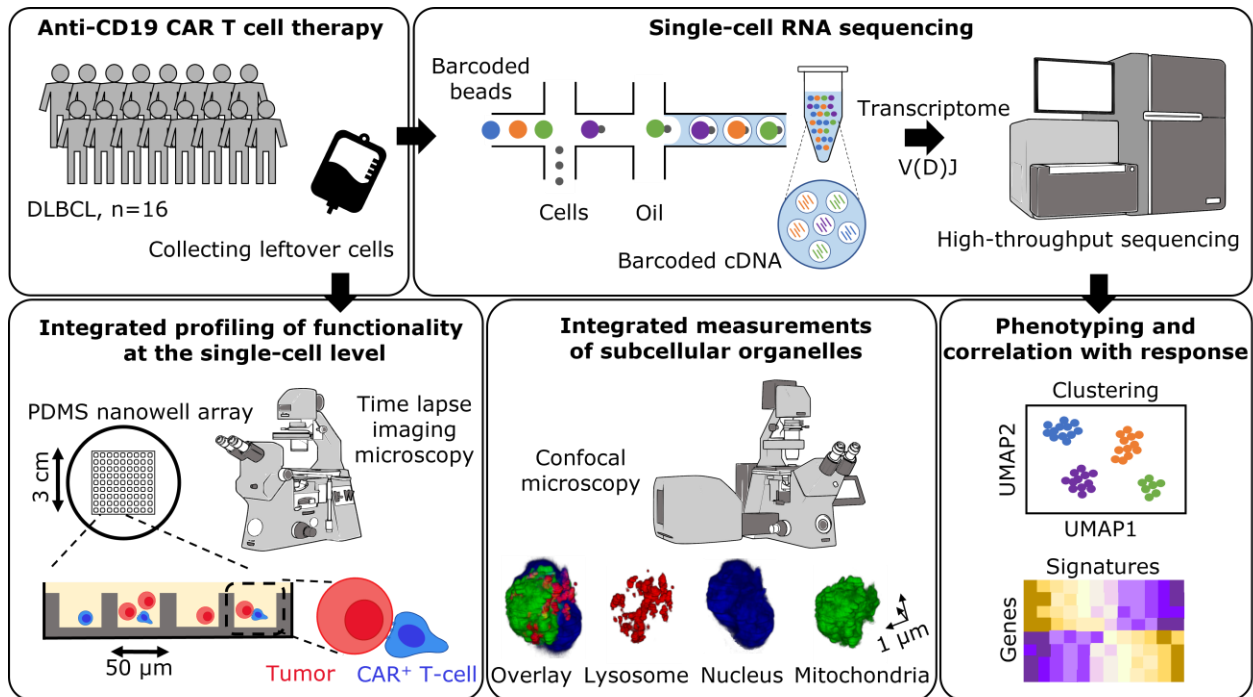
516 **REFERENCES**

- 517 1 Rosenberg, S. A. *et al.* Durable complete responses in heavily pretreated patients with
518 metastatic melanoma using T-cell transfer immunotherapy. *Clin Cancer Res* **17**, 4550-4557,
519 doi:10.1158/1078-0432.CCR-11-0116 (2011).
- 520 2 Maus, M. V. & June, C. H. Making Better Chimeric Antigen Receptors for Adoptive T-cell
521 Therapy. *Clin Cancer Res* **22**, 1875-1884, doi:10.1158/1078-0432.CCR-15-1433 (2016).
- 522 3 Jackson, H. J., Rafiq, S. & Brentjens, R. J. Driving CAR T-cells forward. *Nat Rev Clin*
523 *Oncol* **13**, 370-383, doi:10.1038/nrclinonc.2016.36 (2016).
- 524 4 June, C. H., Riddell, S. R. & Schumacher, T. N. Adoptive cellular therapy: a race to the
525 finish line. *Sci Transl Med* **7**, 280ps287, doi:10.1126/scitranslmed.aaa3643 (2015).
- 526 5 Park, J. H., Geyer, M. B. & Brentjens, R. J. CD19-targeted CAR T-cell therapeutics for
527 hematologic malignancies: interpreting clinical outcomes to date. *Blood* **127**, 3312-3320,
528 doi:10.1182/blood-2016-02-629063 (2016).
- 529 6 Sadelain, M., Riviere, I. & Riddell, S. Therapeutic T cell engineering. *Nature* **545**, 423-431,
530 doi:10.1038/nature22395 (2017).
- 531 7 Rossi, J. *et al.* Preinfusion polyfunctional anti-CD19 chimeric antigen receptor T cells are
532 associated with clinical outcomes in NHL. *Blood* **132**, 804-814, doi:10.1182/blood-2018-
533 01-828343 (2018).
- 534 8 Deng, Q. *et al.* Characteristics of anti-CD19 CAR T cell infusion products associated with
535 efficacy and toxicity in patients with large B cell lymphomas. *Nat Med* **26**, 1878-1887,
536 doi:10.1038/s41591-020-1061-7 (2020).
- 537 9 Sabatino, M. *et al.* Generation of clinical-grade CD19-specific CAR-modified CD8+
538 memory stem cells for the treatment of human B-cell malignancies. *Blood* **128**, 519-528,
539 doi:10.1182/blood-2015-11-683847 (2016).
- 540 10 Singh, N., Perazzelli, J., Grupp, S. A. & Barrett, D. M. Early memory phenotypes drive T
541 cell proliferation in patients with pediatric malignancies. *Sci Transl Med* **8**, 320ra323,
542 doi:10.1126/scitranslmed.aad5222 (2016).
- 543 11 Klebanoff, C. A. *et al.* Determinants of successful CD8+ T-cell adoptive immunotherapy
544 for large established tumors in mice. *Clin Cancer Res* **17**, 5343-5352, doi:10.1158/1078-
545 0432.CCR-11-0503 (2011).
- 546 12 Cherkassky, L. *et al.* Human CAR T cells with cell-intrinsic PD-1 checkpoint blockade
547 resist tumor-mediated inhibition. *J Clin Invest* **126**, 3130-3144, doi:10.1172/JCI83092
548 (2016).
- 549 13 Textor, A. *et al.* Efficacy of CAR T-cell therapy in large tumors relies upon stromal
550 targeting by IFN γ . *Cancer Res* **74**, 6796-6805, doi:10.1158/0008-5472.CAN-14-
551 0079 (2014).
- 552 14 van Bruggen, J. A. C. *et al.* Chronic lymphocytic leukemia cells impair mitochondrial
553 fitness in CD8(+) T cells and impede CAR T-cell efficacy. *Blood* **134**, 44-58,
554 doi:10.1182/blood.2018885863 (2019).
- 555 15 Good, C. R. *et al.* An NK-like CAR T cell transition in CAR T cell dysfunction. *Cell* **184**,
556 6081-6100 e6026, doi:10.1016/j.cell.2021.11.016 (2021).
- 557 16 Bandey, I. N. *et al.* Designed improvement to T-cell immunotherapy by multidimensional
558 single cell profiling. *J Immunother Cancer* **9**, doi:10.1136/jitc-2020-001877 (2021).

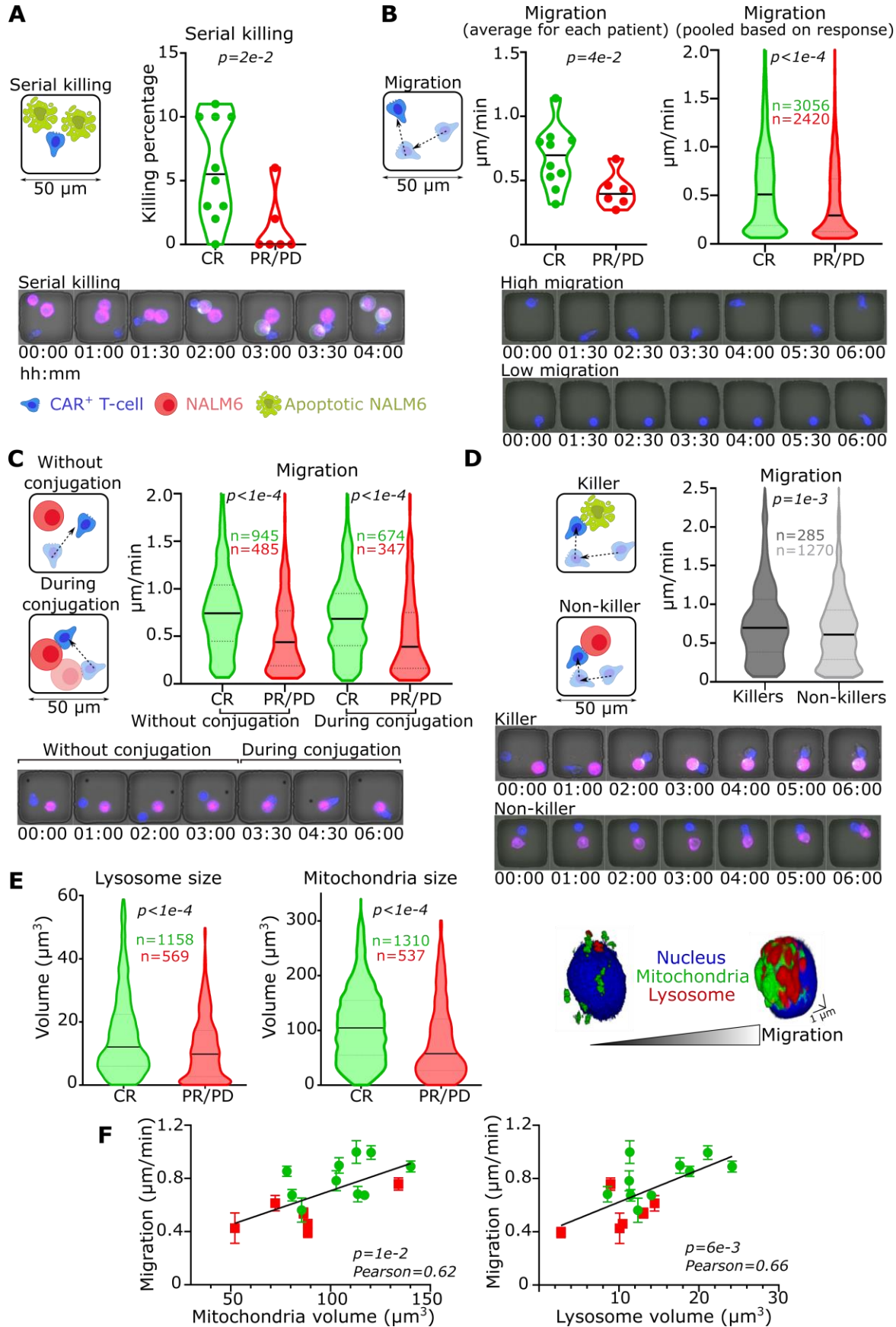
- 559 17 Chen, G. M. *et al.* Integrative Bulk and Single-Cell Profiling of Premanufacture T-cell
560 Populations Reveals Factors Mediating Long-Term Persistence of CAR T-cell Therapy.
561 *Cancer Discov* **11**, 2186-2199, doi:10.1158/2159-8290.CD-20-1677 (2021).
- 562 18 Dupre, L., Houmadi, R., Tang, C. & Rey-Barroso, J. T Lymphocyte Migration: An Action
563 Movie Starring the Actin and Associated Actors. *Front Immunol* **6**, 586,
564 doi:10.3389/fimmu.2015.00586 (2015).
- 565 19 You, R. *et al.* Active surveillance characterizes human intratumoral T cell exhaustion. *J*
566 *Clin Invest* **131**, doi:10.1172/JCI144353 (2021).
- 567 20 Liadi, I. *et al.* Individual Motile CD4(+) T Cells Can Participate in Efficient Multikilling
568 through Conjugation to Multiple Tumor Cells. *Cancer Immunol Res* **3**, 473-482,
569 doi:10.1158/2326-6066.CIR-14-0195 (2015).
- 570 21 Melenhorst, J. J. *et al.* Decade-long leukaemia remissions with persistence of CD4(+) CAR
571 T cells. *Nature* **602**, 503-509, doi:10.1038/s41586-021-04390-6 (2022).
- 572 22 Jacobelli, J. *et al.* Confinement-optimized three-dimensional T cell amoeboid motility is
573 modulated via myosin IIA-regulated adhesions. *Nat Immunol* **11**, 953-961,
574 doi:10.1038/ni.1936 (2010).
- 575 23 Fousek, K. *et al.* CAR T-cells that target acute B-lineage leukemia irrespective of CD19
576 expression. *Leukemia* **35**, 75-89, doi:10.1038/s41375-020-0792-2 (2021).
- 577 24 Bielamowicz, K. *et al.* Trivalent CAR T cells overcome interpatient antigenic variability in
578 glioblastoma. *Neuro Oncol* **20**, 506-518, doi:10.1093/neuonc/nox182 (2018).
- 579 25 Fraietta, J. A. *et al.* Determinants of response and resistance to CD19 chimeric antigen
580 receptor (CAR) T cell therapy of chronic lymphocytic leukemia. *Nat Med* **24**, 563-571,
581 doi:10.1038/s41591-018-0010-1 (2018).
- 582 26 Mrass, P. *et al.* Random migration precedes stable target cell interactions of tumor-
583 infiltrating T cells. *J Exp Med* **203**, 2749-2761, doi:10.1084/jem.20060710 (2006).
- 584 27 Breart, B., Lemaitre, F., Celli, S. & Bousso, P. Two-photon imaging of intratumoral CD8+
585 T cell cytotoxic activity during adoptive T cell therapy in mice. *J Clin Invest* **118**, 1390-
586 1397, doi:10.1172/JCI34388 (2008).
- 587 28 Boulch, M. *et al.* A cross-talk between CAR T cell subsets and the tumor microenvironment
588 is essential for sustained cytotoxic activity. *Sci Immunol* **6**,
589 doi:10.1126/sciimmunol.abd4344 (2021).
- 590 29 Zinselmeyer, B. H. *et al.* PD-1 promotes immune exhaustion by inducing antiviral T cell
591 motility paralysis. *J Exp Med* **210**, 757-774, doi:10.1084/jem.20121416 (2013).
- 592 30 Bhat, P., Leggatt, G., Waterhouse, N. & Frazer, I. H. Interferon-gamma derived from
593 cytotoxic lymphocytes directly enhances their motility and cytotoxicity. *Cell Death Dis* **8**,
594 e2836, doi:10.1038/cddis.2017.67 (2017).
- 595 31 Krummel, M. F., Bartumeus, F. & Gerard, A. T cell migration, search strategies and
596 mechanisms. *Nat Rev Immunol* **16**, 193-201, doi:10.1038/nri.2015.16 (2016).
- 597 32 Hammer, J. A., Wang, J. C., Saeed, M. & Pedrosa, A. T. Origin, Organization, Dynamics,
598 and Function of Actin and Actomyosin Networks at the T Cell Immunological Synapse.
599 *Annu Rev Immunol* **37**, 201-224, doi:10.1146/annurev-immunol-042718-041341 (2019).
- 600 33 Menard, C. *et al.* Lenalidomide triggers T-cell effector functions in vivo in patients with
601 follicular lymphoma. *Blood Adv* **5**, 2063-2074, doi:10.1182/bloodadvances.2020003774
602 (2021).
- 603 34 Aue, G. *et al.* Lenalidomide-induced upregulation of CD80 on tumor cells correlates with
604 T-cell activation, the rapid onset of a cytokine release syndrome and leukemic cell clearance

- 605 in chronic lymphocytic leukemia. *Haematologica* **94**, 1266-1273,
606 doi:10.3324/haematol.2009.005835 (2009).
- 607 35 Ramsay, A. G. *et al.* Chronic lymphocytic leukemia cells induce defective LFA-1-directed
608 T-cell motility by altering Rho GTPase signaling that is reversible with lenalidomide. *Blood*
609 **121**, 2704-2714, doi:10.1182/blood-2012-08-448332 (2013).
- 610 36 Wang, Z. *et al.* Lenalidomide Enhances CAR-T Cell Activity Against Solid Tumor Cells.
611 *Cell Transplant* **29**, 963689720920825, doi:10.1177/0963689720920825 (2020).
- 612 37 Ramsay, A. G. *et al.* Chronic lymphocytic leukemia T cells show impaired immunological
613 synapse formation that can be reversed with an immunomodulating drug. *J Clin Invest* **118**,
614 2427-2437, doi:10.1172/JCI35017 (2008).
- 615 38 Kawalekar, O. U. *et al.* Distinct Signaling of Coreceptors Regulates Specific Metabolism
616 Pathways and Impacts Memory Development in CAR T Cells. *Immunity* **44**, 380-390,
617 doi:10.1016/j.immuni.2016.01.021 (2016).
- 618 39 van der Windt, G. J. *et al.* Mitochondrial respiratory capacity is a critical regulator of CD8+
619 T cell memory development. *Immunity* **36**, 68-78, doi:10.1016/j.immuni.2011.12.007
620 (2012).
- 621 40 Schaffer, B. E. *et al.* Identification of AMPK Phosphorylation Sites Reveals a Network of
622 Proteins Involved in Cell Invasion and Facilitates Large-Scale Substrate Prediction. *Cell*
623 *Metab* **22**, 907-921, doi:10.1016/j.cmet.2015.09.009 (2015).
- 624 41 Georgiadou, M. *et al.* AMPK negatively regulates tensin-dependent integrin activity. *J Cell*
625 *Biol* **216**, 1107-1121, doi:10.1083/jcb.201609066 (2017).
- 626 42 Zhang, L. *et al.* Lineage tracking reveals dynamic relationships of T cells in colorectal
627 cancer. *Nature* **564**, 268-272, doi:10.1038/s41586-018-0694-x (2018).
- 628 43 Jiao, S. *et al.* Intratumor expanded T cell clones can be non-sentinel lymph node derived in
629 breast cancer revealed by single-cell immune profiling. *J Immunother Cancer* **10**,
630 doi:10.1136/jitc-2021-003325 (2022).
- 631 44 Bhatt, D. *et al.* STARTRAC analyses of scRNAseq data from tumor models reveal T cell
632 dynamics and therapeutic targets. *J Exp Med* **218**, doi:10.1084/jem.20201329 (2021).
- 633 45 Bai, Z. *et al.* Single-cell antigen-specific landscape of CAR T infusion product identifies
634 determinants of CD19-positive relapse in patients with ALL. *Sci Adv* **8**, eabj2820,
635 doi:10.1126/sciadv.abj2820 (2022).
- 636 46 Hung, W. C. *et al.* Distinct signaling mechanisms regulate migration in unconfined versus
637 confined spaces. *J Cell Biol* **202**, 807-824, doi:10.1083/jcb.201302132 (2013).
- 638 47 Liadi, I., Roszik, J., Romain, G., Cooper, L. J. & Varadarajan, N. Quantitative high-
639 throughput single-cell cytotoxicity assay for T cells. *J Vis Exp*, e50058, doi:10.3791/50058
640 (2013).
- 641 48 An, X. *et al.* Single-cell profiling of dynamic cytokine secretion and the phenotype of
642 immune cells. *PLoS One* **12**, e0181904, doi:10.1371/journal.pone.0181904 (2017).
- 643 49 Romain, G. *et al.* Antibody Fc engineering improves frequency and promotes kinetic
644 boosting of serial killing mediated by NK cells. *Blood* **124**, 3241-3249, doi:10.1182/blood-
645 2014-04-569061 (2014).
- 646 50 Tinevez, J. Y. *et al.* TrackMate: An open and extensible platform for single-particle
647 tracking. *Methods* **115**, 80-90, doi:10.1016/j.ymeth.2016.09.016 (2017).
- 648 51 Hao, Y. *et al.* Integrated analysis of multimodal single-cell data. *Cell* **184**, 3573-3587
649 e3529, doi:10.1016/j.cell.2021.04.048 (2021).
- 650 52 Huang, M. *et al.* SAVER: gene expression recovery for single-cell RNA sequencing. *Nat*
651 *Methods* **15**, 539-542, doi:10.1038/s41592-018-0033-z (2018).

- 652 53 Hanzelmann, S., Castelo, R. & Guinney, J. GSVA: gene set variation analysis for
653 microarray and RNA-seq data. *BMC Bioinformatics* **14**, 7, doi:10.1186/1471-2105-14-7
654 (2013).
- 655 54 Jena, B. *et al.* Chimeric antigen receptor (CAR)-specific monoclonal antibody to detect
656 CD19-specific T cells in clinical trials. *PLoS One* **8**, e57838,
657 doi:10.1371/journal.pone.0057838 (2013).
- 658 55 Singh, H. *et al.* Reprogramming CD19-specific T cells with IL-21 signaling can improve
659 adoptive immunotherapy of B-lineage malignancies. *Cancer Res* **71**, 3516-3527,
660 doi:10.1158/0008-5472.CAN-10-3843 (2011).
- 661



662
663 **Figure 1. Study design for integrated single-cell multi-omic profiling of patients' infusion**
664 **products.**
665 Schematic overview of the experimental design for profiling the residual CAR T cell infusion
666 products of 16 DLBCL patients (10 CR, 6 PR/PD). Cells were used for scRNA-seq analysis, confocal
667 microscopy, and Timelapse Imaging Microscopy In Nanowell Grids (TIMING).



669 **Figure 2. T cells from CR patients were enriched for migration, serial killing, and**
670 **mitochondrial volume; in comparison to T cells from PR/PD.**

671 (A) Schematic of a serial killing event wherein a CAR T cell conjugates and kills two NALM-6
672 cells. The plot on the right shows the comparison between T cells from either CR or PR/PD
673 in terms of serial killing within all 1E:2T nanowells. Micrograph showing an example of a
674 serial killing event through the 6-hours (hh:mm) time-lapse imaging. Examples of mono-
675 killing and no-killing events are provided in supplementary figure 1.

676 (B) Schematic of migration for a single CAR T cell (1E:0T). The plots on the right illustrate the
677 comparison between migration of T cells from either CR or PR/PD within all nanowells with
678 1E:0T. On the left plot, each dot represents the average T-cell migration for each patient,
679 while the plot on the right shows the comparison between all T cells from CR and T cells
680 from PR/PD. Micrograph showing examples of a T-cell with high (2 $\mu\text{m}/\text{min}$) and a low
681 migratory capacity (0.2 $\mu\text{m}/\text{min}$).

682 (C) Schematic of migration for a CAR T cell next to a NALM-6 cell (1E:1T) in two conditions:
683 during the conjugation of CAR T and NALM-6 and when they are unconjugated. Plot
684 showing the comparison between the migration of CR and PR/PD CAR T cells within all
685 nanowells with 1E:1T without or during the conjugation. Micrograph showing an example
686 of a CAR T cell migration before and during the conjugation with a NALM-6 cell. Not all the
687 CAR T cells make conjugation with NALM-6.

688 (D) Schematic of migration of a CAR T cell before conjugation with NALM-6 cell (1E:1T) in killer
689 and non-killer CAR T cells. The plots on the right show the comparison between migration
690 (prior to conjugation) of killer and non-killer CAR T cells within all nanowells with 1E:1T

691 where conjugation happens (regardless of response). Micrographs showing examples of a
692 killer CAR T cell and a non-killer CAR T cell.

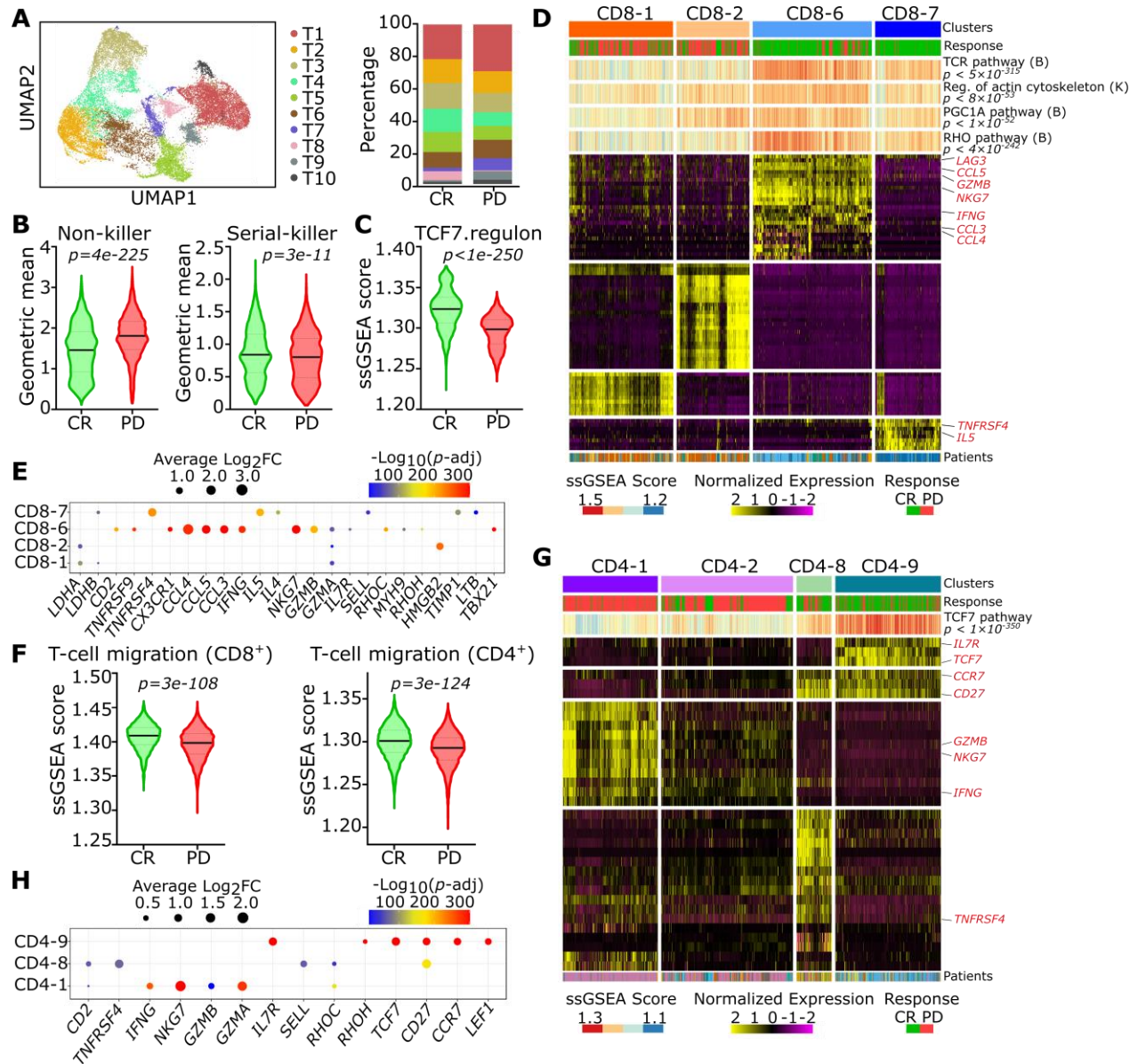
693 (E) Comparison of mitochondria and lysosome size between CR and PR/PD T cells. The
694 confocal 3D image represents the correlation between mitochondria/lysosome size and
695 migration of the CAR T cells. The nucleus is shown in blue, mitochondria in green, and
696 lysosome in red.

697 (F) Plots showing the correlation between average organelle size and average migration (1E:1T,
698 without conjugation) of T cells. Each dot represents an IP product. *P* value and Pearson
699 correlation were calculated for the linear regression. Error bars represents SEM.

700 The black bar represents the median, and the dotted lines denote quartiles in violin plots. *P* values
701 were computed using Mann-Whitney tests.

702

703



704

705 **Figure 3. Transcriptional profiling of CAR T infusion products associated with response**
 706 **revealed by single-cell RNA sequencing.**

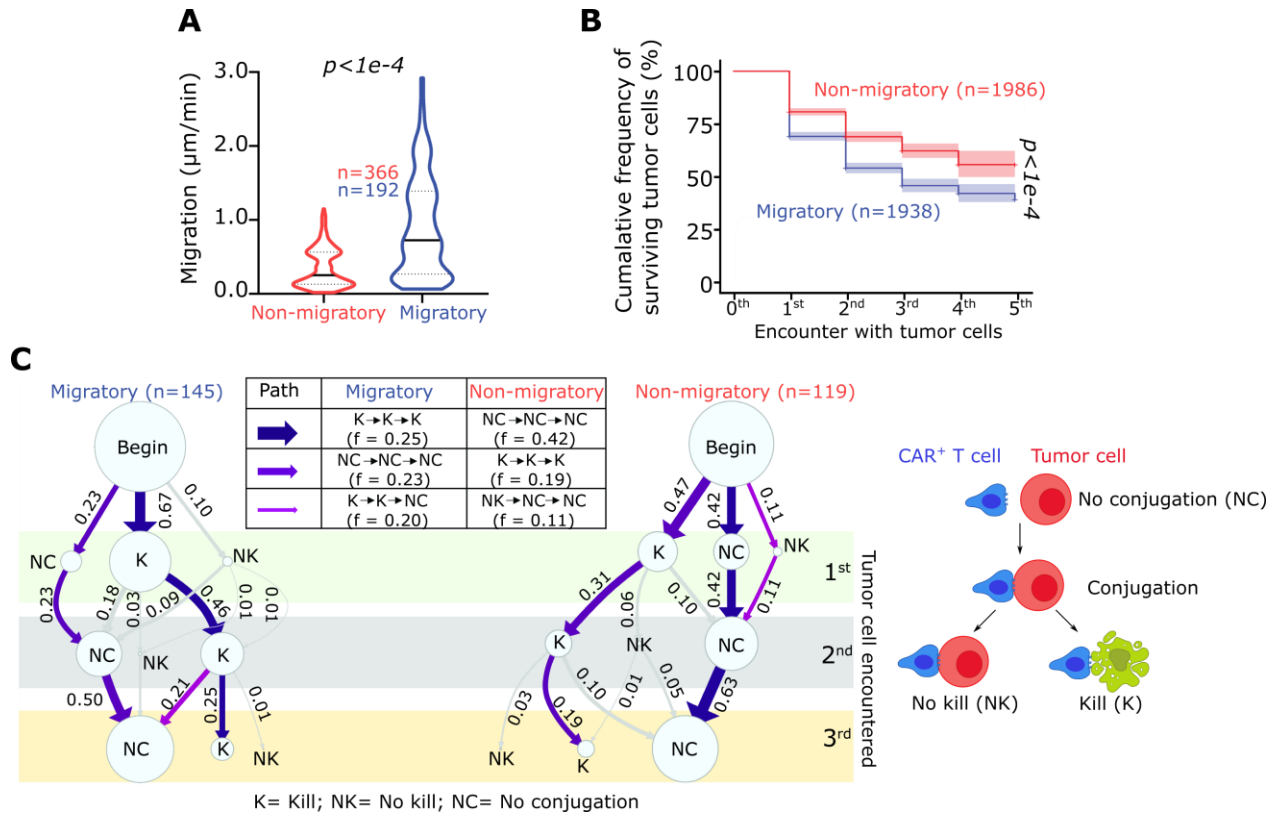
707 (A) Uniform Manifold Approximation and Projection (UMAP) for 21,469 cells from nine IPs. Bar
 708 plot showing the distribution of T cells from CR and PD/PR among 10 clusters determined
 709 using unsupervised clustering.

- 710 (B) Comparison between CD8⁺ T cells from CR and PD for non-killer (*GZMA* and *CD69*)
711 signatures or serial-killer (*CD2* and *CD27*) T cells.
- 712 (C) Comparison between CD8⁺ T cells from CR and PD for TCF7 regulon signatures calculated
713 using ssGSEA.
- 714 (D) Heat map of four CD8⁺ T cell clusters generated by unsupervised clustering. CD8-1 and
715 CD8-2 contain mostly cells from PD while CD8-6 and CD8-7 are enriched with CR cells. A
716 color-coded track on top shows the cells from infusion products of CR (green) and PD (red).
717 Additional tracks show the ssGSEA scores of TCR, actin cytoskeleton regulation, PGC1A,
718 and RHO pathways, respectively. B: BIOCARTA and K: KEGG show the source for the
719 pathways. These pathways are significantly enriched in CR clusters compared to PD clusters.
720 The track below the heatmap shows the sample origin for each cell.
- 721 (E) Bubble plot showing key genes differentially expressed among four CD8⁺ T clusters.
- 722 (F) Comparing ssGSEA-derived migration score between T cells from CR and PD for either
723 CD4⁺ T cells or CD8⁺ T cells.
- 724 (G) Heat map of four CD4⁺ T cell clusters generated by unsupervised clustering. CD4-1 and
725 CD4-2 contain mostly cells from PD while CD4-8 and CD4-9 are enriched with CR cells. A
726 color-coded track on top shows the cells from infusion products of CR (green) and PD (red).
727 Additional track shows the ssGSEA scores for TCF7 regulon pathway which is significantly
728 enriched in CR clusters compared to PD clusters. The track below the heatmap, shows the
729 sample origin for each cell.
- 730 (H) Bubble plot showing key genes differentially expressed among CD4⁺ T clusters.

731 For violin plots, the black bar represents the median and the dotted lines denote quartiles. *P* values

732 for both heatmaps and violin plots were computed using Wilcoxon tests.

733



734

735 **Figure 4. Enrichment and functional characterization of migratory 19-28z T cells.**

736 (A) Comparisons between the migration of migrated (migratory) and non-migrated (non-

737 migratory) cells. The black bar represents the median and the dotted lines denote quartiles.

738 P value were computed using Mann-Whitney tests.

739 (B) Sustained killing mediated by individual migratory 19-28z T cells ordered by the encounter

740 with tumor cells. Error bars indicate 95 % CI. P value was computed using log-rank test.

741 (C) State transition diagram illustrating the evolution of the interaction between 19-28z T

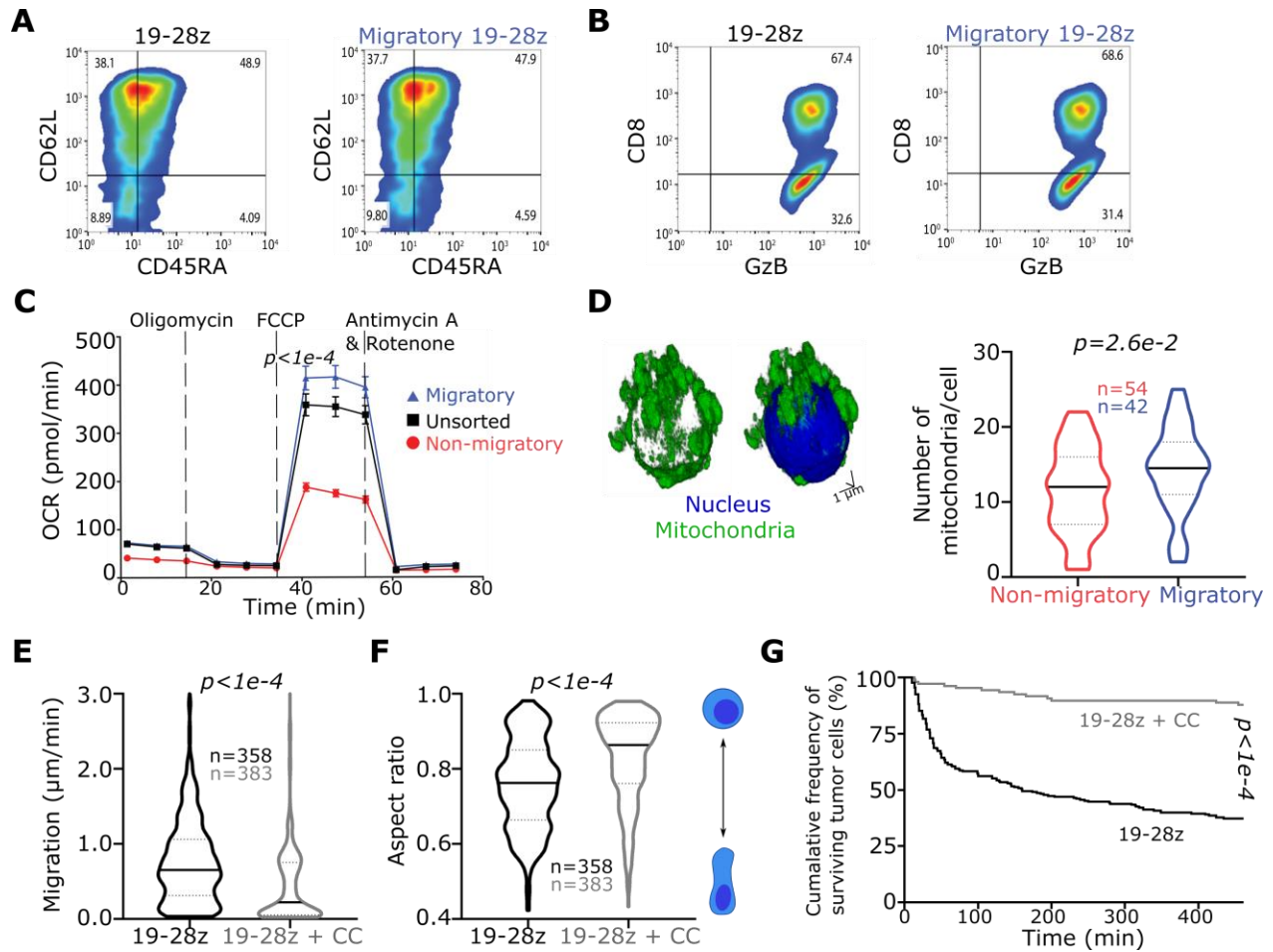
742 cells and tumor cells within single-cell assays. The thickness of the lines connecting the

743 state is proportional to the frequency of the transition. The data was obtained from

744 nanowells containing exactly one T cell and 3-5 tumor cells. All P values were computed

745 using Mann-Whitney tests and each dot represents a single effector cell. All data shown

746 here are from one representative population derived from at least three independent
747 healthy donor-derived 19-28z T cells.



748

749 **Figure 5. The phenotype and bioenergetics of migratory CAR T cells.**

750 (A/B) The phenotype (A) and Granzyme B (GzB) expression (B) of the migratory and unsorted 19-
 751 28z T cells as determined by flow cytometry.

752 (C) Basal OCR levels measured for three different 19-28z T cell populations. *P* value is for
 753 comparison of the SRC comparing the migratory and non-migratory subsets using multiple
 754 t tests.

755 (D) A confocal 3D image of a migratory 19-28z T cell. Nuclei are shown in blue and
 756 mitochondria in green. The plot shows the number of mitochondria per cell compared
 757 between migratory and non-migratory 19-28z T cells.

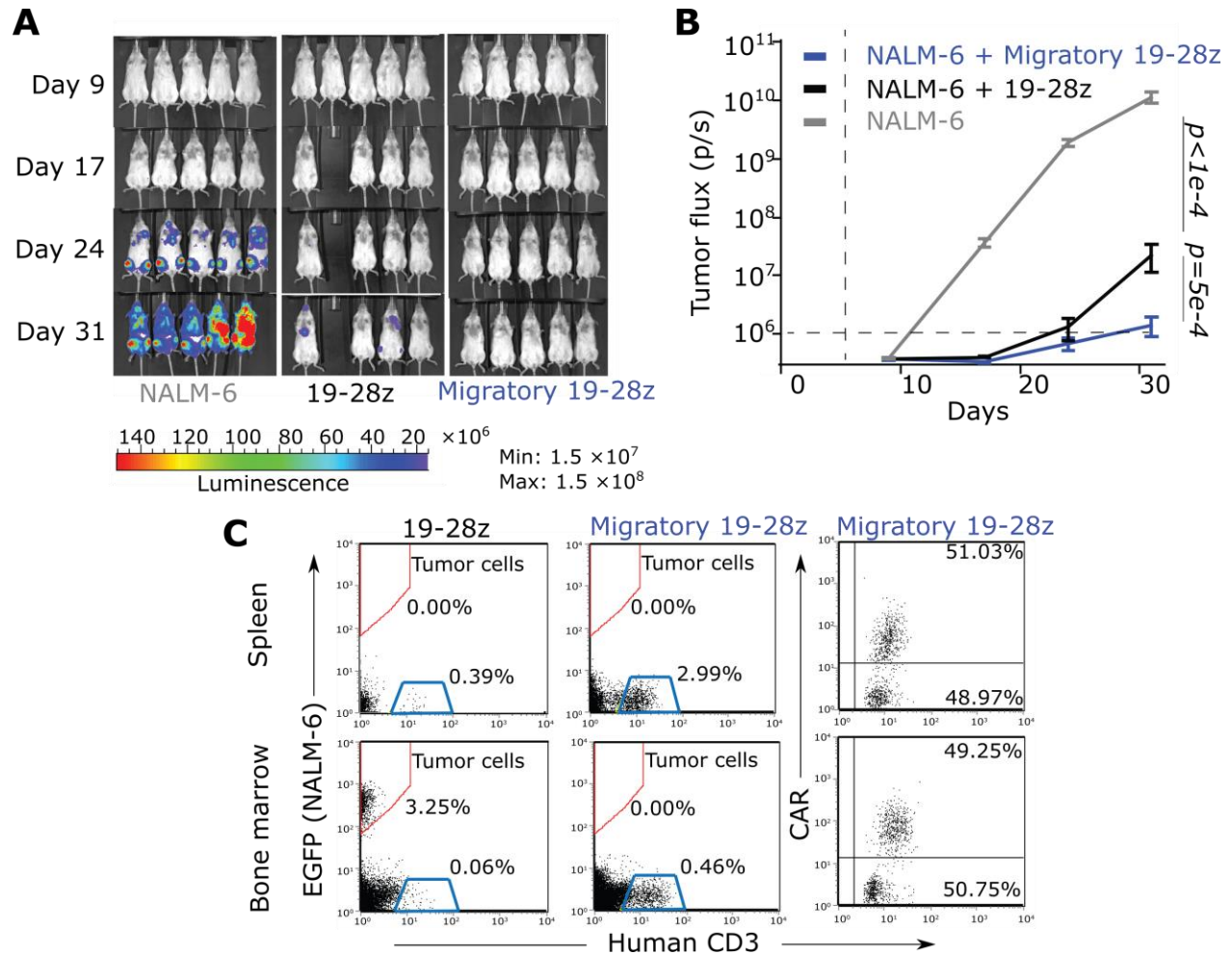
758 (E/F) The migration and polarization of 19-28z T cells treated with Compound C (CC). All data
759 representative of at least three independent experiments performed with cells from at least
760 three healthy human donors-derived 19-28z T cells. The black bar represents the median
761 and the dotted lines denote quartiles. The *P* value was computed using a Mann-Whitney
762 test.

763 (G) Comparisons of the killing frequency of vehicle treated (DMSO) or CC treated 19-28z CAR
764 T cells. Each data point represents a single-cell. *P* value was computed using log-rank test.

765

766

767



768

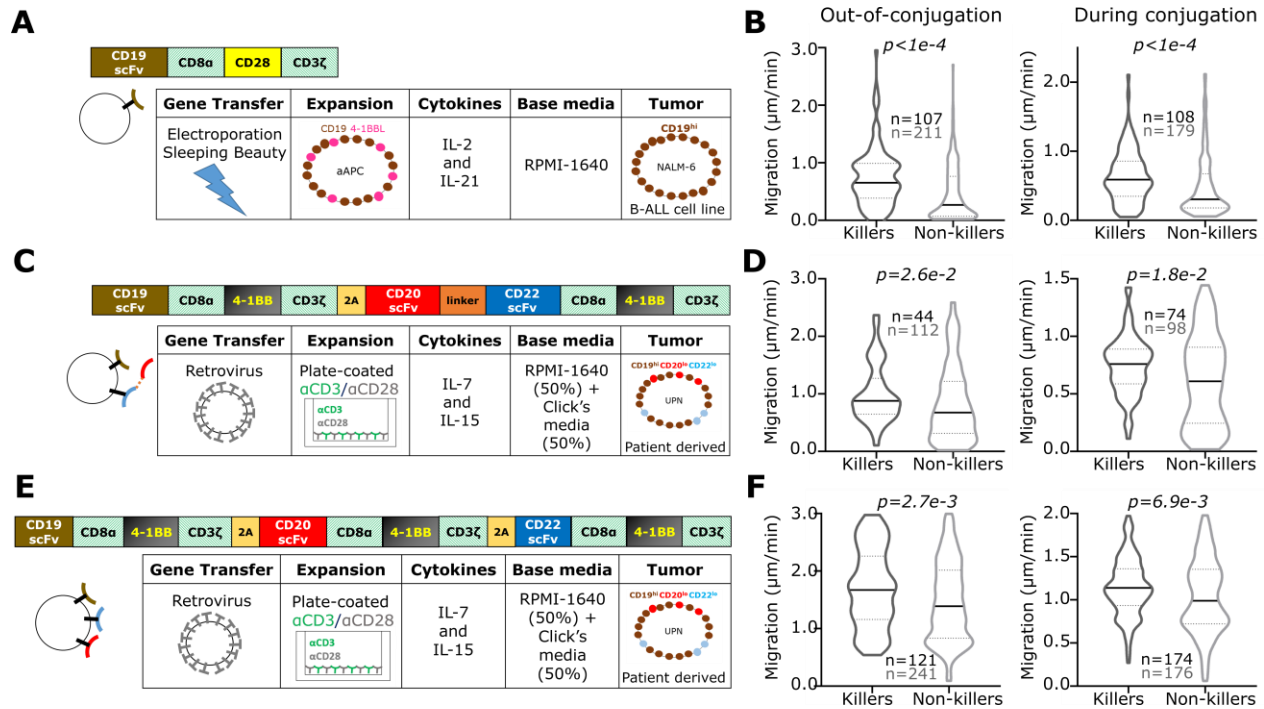
769 **Figure 6. Migratory 19-28 T cells reject established leukemia and sustain persistence in vivo.**

770 (A) False-colored images illustrating the photon flux from ffLuc expressing EGFP⁺NALM-6 cells.

771 (B) Time course of the longitudinal measurements of NALM-6 derived photon flux from the
772 three separate cohorts of mice (n = 10 in each group). The background luminescence was
773 defined based on mice with no tumor. Error bars represent SEM and P values are computed
774 using the Mann-Whitney test.

775 (C) On day 31, four mice from each group were euthanized, and tissues (bone marrow and
776 spleen) were harvested and analyzed by flow cytometry for expression of human CD3
777 (human T cells) and EGFP (gated within hCD19 cells). The CAR⁺ T cells were identified by a

778 scFv-specific antibody, as described previously⁵⁴. The flow data is representative from one
779 mouse in each group.



780

781 **Figure 7. Quantifying the link between migration and functionality in diverse CARs.**

782 (A, C and E) Schematic illustrating the CAR structure, manufacturing and expansion, and the target
783 cells used for profiling functionality of individual CAR⁺ T cells using TIMING.

784 (B, D and F) The migration of individual killer and non-killer CAR T cells without and with
785 conjugation to tumor cells. All data from an E:T of 1:1. The black bar represents the
786 median and the dotted lines denote quartiles. All *P* values were computed using
787 Mann-Whitney tests and each data point represents a single effector cell.